nature materials

LETTERS

PUBLISHED ONLINE: 11 APRIL 2016 | DOI: 10.1038/NMAT4621

Enhanced ethylene separation and plasticization resistance in polymer membranes incorporating metal–organic framework nanocrystals

Jonathan E. Bachman[1], Zachary P. Smith[2], Tao Li[3], Ting Xu[2,3,4] and Jeffrey R. Long[1,2,4]*

The implementation of membrane-based separations in the petrochemical industry has the potential to reduce energy consumption significantly relative to conventional separation processes[1]. Achieving this goal, however, requires the development of new membrane materials with greater selectivity, permeability and stability than available at present. Here, we report composite materials consisting of nanocrystals of metal–organic frameworks dispersed within a high-performance polyimide, which can exhibit enhanced selectivity for ethylene over ethane, greater ethylene permeability and improved membrane stability. Our results suggest that framework–polymer interactions reduce chain mobility of the polymer while simultaneously boosting membrane separation performance. The increased stability, or plasticization resistance, is expected to improve membrane utility under real process conditions for petrochemical separations and natural gas purification. Furthermore, this approach can be broadly applied to numerous polymers that encounter aggressive environments, potentially making gas separations possible that were previously inaccessible to membranes.

Separations in the petrochemical industry are extremely energy intensive, and improving process efficiency has the potential to create significant cost and environmental savings[1]. One of the most challenging industrial gas separations is the purification of olefins from olefin/paraffin mixtures, which is accomplished today by cryogenic distillation and accounts for 120 Tbtu/year in energy consumption[1,2]. Membranes have been proposed as supplements to conventional distillation, and although numerous membrane materials have shown promise for olefin/paraffin separation, there are no materials with adequate separation performance under realistic process conditions[3,4]. Indeed, this materials challenge extends to numerous other gas separations, including the purification of natural gas and the production of other petrochemicals[4]. In particular, the limitation of membrane technology is due to a lack of materials that have a combination of high selectivity, permeability, processability and stability during operation, all of which are necessary for implementation of a material. Molecular sieve-based membranes can achieve high selectivities and permeabilities, but are difficult to fabricate on a large scale[5–7], or are prone to defects[8]. Similarly, thermally rearranged polymer membranes can exhibit excellent separation performance, but are brittle and susceptible to breaking during operation[9]. Classical polymer membranes are robust and processable, but these generally do not exhibit sufficiently high olefin/paraffin selectivity and permeability, and, perhaps more importantly, their performance diminishes rapidly with use owing to plasticization. Plasticization, which involves a marked and often unpredictable loss in selectivity as a result of polymer swelling on exposure to high pressures of polarizable gases, is a major obstacle to the commercial adoption of membranes for refinery separations or natural gas purification. Current strategies for reducing plasticization rely on polymer crosslinking, which is limited to polymers with crosslinkable organic functionalities and often has the deleterious effect of reducing membrane permeability[10]. The approach we adopt here is to create potential crosslinks within a high-performance polymer by incorporating nanocrystals of metal–organic frameworks containing coordinatively unsaturated metal sites, which are in and of themselves expected to exhibit an improved separation performance[11]. As we will demonstrate, the resulting composites can uniquely and simultaneously satisfy the requirements of high selectivity, permeability, processability and stability.

Metal–organic frameworks are porous crystalline materials that have shown promise for a variety of gas separations, including for key hydrocarbon separations[11]. Traditionally developed for adsorption-based separations, metal–organic frameworks have more recently shown promise for use in membranes[12]. These materials have been formed into composite films by mixing with polymers[13–16] and tested as stand-alone membranes in the form of hollow fibres[8] or sheets[17]. Although they have been successfully employed for improving propylene/propane[13] and CO_2 separations[14,18,19], this approach has, until now, not significantly improved ethylene/ethane selectivity and permeability[3,20], nor has it been shown to enhance membrane stability. For polymer membranes, ethane adsorption is nearly identical to that of ethylene, thereby preventing improvements in selectivity based on a sorption-selectivity mechanism[21]. In contrast, many adsorbents with coordinatively unsaturated metal sites have enhanced adsorptive affinity for olefins over paraffins owing to a strong interaction between the metal and the π-system of the alkene[13,22,23]. Indeed, these interactions have led to record-high adsorption selectivities and capacities in the metal–organic frameworks M_2(dobdc) (M-MOF-74; CPO-27-M; M = Mg, Mn, Fe, Co, Ni, Zn; $dobdc^{4-}$ = 2,5-dioxido-1,4-benzenedicarboxylate), which feature ∼12 Å-wide hexagonal channels lined with a high concentration of exposed divalent metal cations[24–27].

To achieve an intimate dispersion and test their influence on ethylene/ethane separation performance in polymer composites, a

[1]Department of Chemical and Biomolecular Engineering, University of California, Berkeley, California 94720, USA. [2]Department of Chemistry, University of California, Berkeley, California 94720, USA. [3]Department of Materials Science, University of California, Berkeley, California 94720, USA. [4]Materials Sciences Division, Lawrence Berkeley National Laboratory, Berkeley, California 94720, USA. *e-mail: jrlong@berkeley.edu

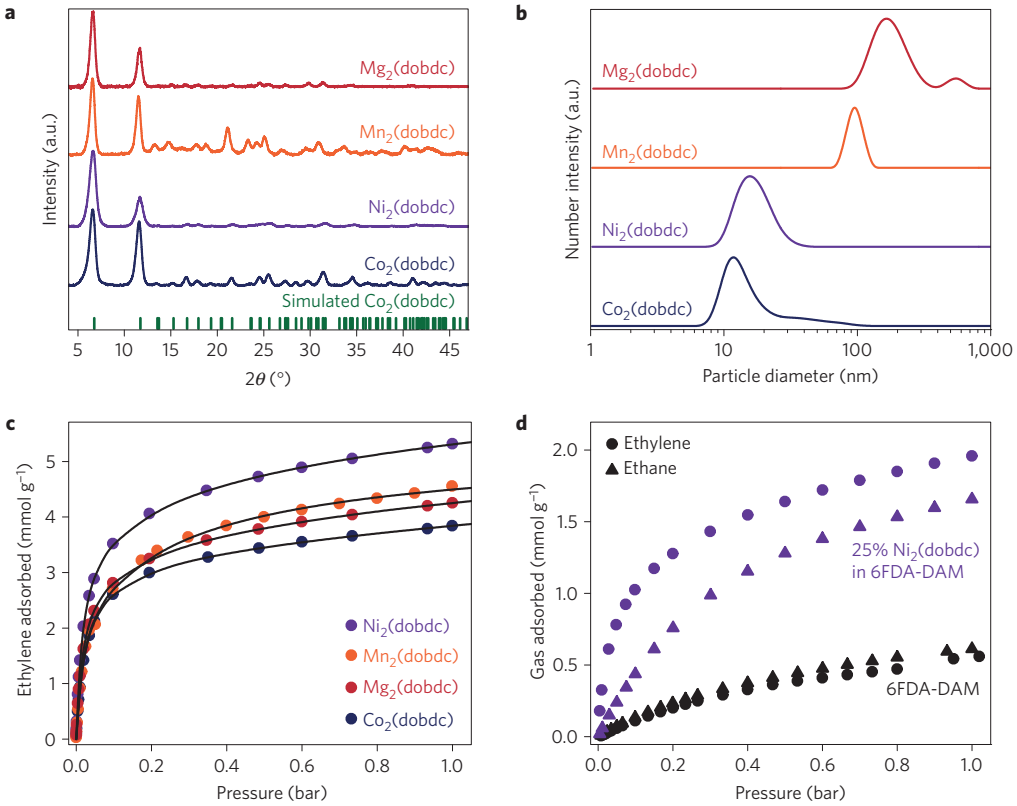

Figure 1 | Physical and adsorptive properties for M_2(dobdc) nanocrystals. a, X-ray powder diffraction was used to confirm the crystallinity and phase purity of all as-synthesized M_2(dobdc) nanocrystals. Vertical lines indicate a simulated pattern for Co_2(dobdc). **b**, Number-weighted particle size distributions, as measured by dynamic light scattering. **c**, Ethylene adsorption isotherms and their corresponding dual-site Langmuir fits (black lines) at 35 °C. **d**, Ethylene (circles) and ethane (triangles) adsorption isotherms at 35 °C for the neat 6FDA-DAM polymer and a film loaded with 25 wt% Ni_2(dobdc).

series of M_2(dobdc) (M = Mg, Mn, Co, Ni) nanocrystals were synthesized (Fig. 1a). As measured by dynamic light scattering, the mean particle sizes for Co_2(dobdc) and Ni_2(dobdc) were found to be 17 ± 3 and 18 ± 5 nm, respectively, whereas Mn_2(dobdc) and Mg_2(dobdc) tended to form much larger nanoparticles of 100 ± 20 and 200 ± 50 nm, respectively (Fig. 1b). Particle sizes were confirmed by scanning electron microscopy and transmission electron microscopy (Supplementary Fig. 1). From a practical point of view, polymer membranes that are currently used in industry are very thin (~100 nm), so dispersed particles in these films would need to be smaller than the thickness of the films. For such nanocrystal/polymer composites to maintain processability, particles with dimensions much less than 100 nm would probably be required, which is the case for Ni_2(dobdc) and Co_2(dobdc). The nanocrystalline frameworks exhibit high ethylene adsorption capacity (Fig. 1c) as well as ethylene/ethane selectivity (Supplementary Fig. 2). For the polymer phase of the membrane, we chose a high-performance polyimide, 6FDA-DAM (6FDA = 4,4′-(hexafluoroisopropylidene)diphthalic anhydride; DAM = 2,4,6-trimethyl-1,3-phenylenediamine), which has been identified as a promising material for olefin/paraffin separations on the basis of a high olefin permeability and a high olefin/paraffin selectivity that place it near the predicted upper bound for a pure polymer membrane[28].

For each nanocrystal type studied, the amount of gas adsorbed in the composite film corresponds to the weighted average between the neat polyimide and the pure nanocrystals, indicating that the exposed metal cations of M_2(dobdc) are fully accessible to ethylene and ethane (Supplementary Fig. 3). Gas adsorption experiments performed on neat 6FDA-DAM compared to 6FDA-DAM loaded with 25 wt% Ni_2(dobdc) revealed that the presence of Ni_2(dobdc) increases the amount of both ethylene and ethane adsorbed, while also introducing a marked adsorption selectivity for ethylene (Fig. 1d). Overall, the adsorption isotherms indicate that, in equilibrium with the upstream pressure, a higher concentration of gas is dissolved in the film for the M_2(dobdc)/6FDA-DAM membranes relative to the neat polymer. This causes a steeper concentration gradient within M_2(dobdc)/6FDA-DAM membranes, and thus a greater driving force for transport and higher permeabilities.

Single-component ethylene and ethane permeation measurements were performed on a neat 6FDA-DAM membrane, as well as on M_2(dobdc)/6FDA-DAM composites with different M_2(dobdc) loadings (Fig. 2a). In particular, incorporating Ni_2(dobdc) or Co_2(dobdc) into 6FDA-DAM significantly improves the gas separation performance. With 25 wt% Ni_2(dobdc) and 33 wt% Co_2(dobdc), selectivities for ethylene over ethane nearly doubled, increasing from 2.7 for the pure polymer to 4.6 and 5.0, respectively, while ethylene permeabilities improved by factors of 2.6 and 5.3, respectively. The increased permeation rates for ethylene and ethane indicate that the adsorbed phase is mobile, and that gases transport rapidly between the nanocrystal and polymer phases. By applying results from gas adsorption and permeation to the solution-diffusion model, the relevant effective solubility and diffusivity parameters were obtained. We found that the solubility of both gases increases and solubility selectivity is increased from 0.86 in 6FDA-DAM to 1.32 in 25 wt% Ni_2(dobdc) while the diffusivity of ethylene is also increased without losses in diffusivity selectivity. Indeed, this places these membranes well above the polymer upper bound for ethylene/ethane, a particularly challenging membrane separation. Such increases in selectivity

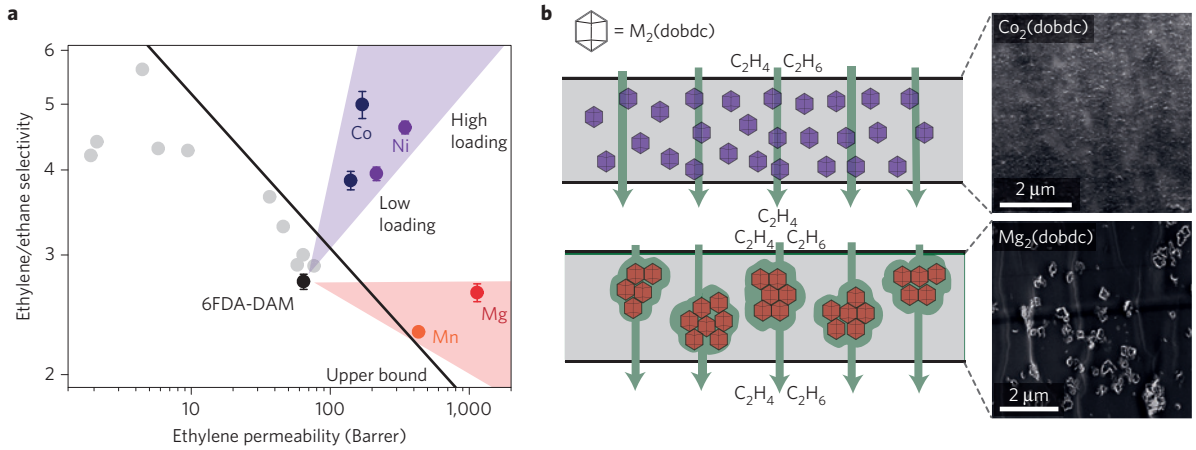

Figure 2 | Ethylene/ethane separation performance for M_2(dobdc)/6FDA-DAM membranes. a, Membrane performance at 2 bar feed pressure and 35 °C relative to the upper bound for polymers. Membrane loadings by weight are 10% and 33% for Co_2(dobdc), 6% and 25% for Ni_2(dobdc), 23% for Mg_2(dobdc), and 13% for Mn_2(dobdc). Uncertainty in selectivity represents propagation of uncertainty in permeability based on two independent membrane samples, and each sample was measured twice to ensure no plasticization or conditioning effects. Grey circles represent neat polymers from the literature. **b**, TEM images of 33% Co_2(dobdc) and 23% Mg_2(dobdc) membrane cross-sections and corresponding illustrations of the proposed gas transport mechanisms, where purple hexagons represent Co_2(dobdc) or Ni_2(dobdc) nanocrystals and red hexagons represent Mg_2(dobdc) or Mn_2(dobdc) nanocrystals.

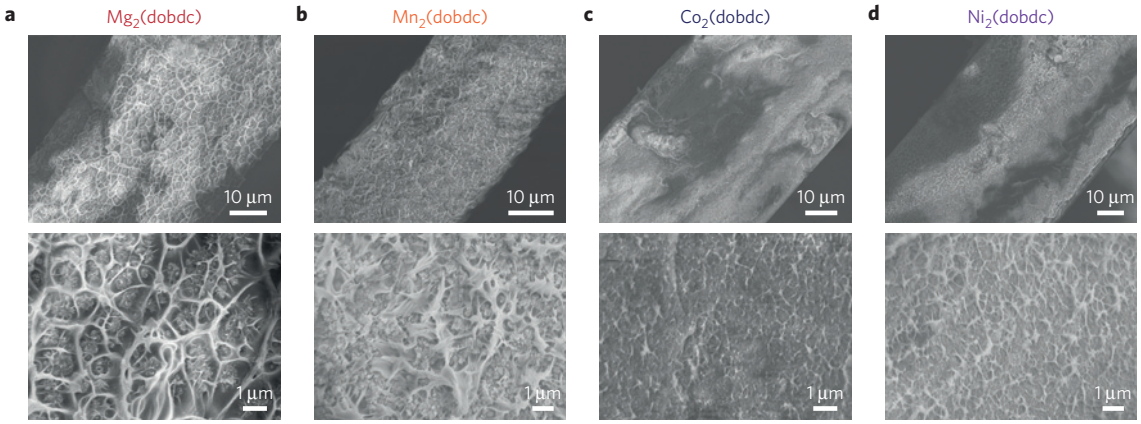

Figure 3 | Cross-sectional images of M_2(dobdc)/6FDA-DAM membranes. Scanning electron micrographs for **a**, Mg_2(dobdc), **b**, Mn_2(dobdc), **c**, Co_2(dobdc) and **d**, Ni_2(dobdc).

and permeability would translate to higher-purity olefins produced using a lower membrane area, pushing membrane technology closer to commercial applicability. In contrast, Mg_2(dobdc) and Mn_2(dobdc) did not show improvements in ethylene/ethane selectivity. Instead, there were increases in both ethylene and ethane permeabilities and diffusivities, leading to decreases in permselectivity and diffusive selectivity (Supplementary Table 1). It is likely that the smaller particle sizes, and accompanying higher external surface areas, for Ni_2(dobdc) and Co_2(dobdc) lead to a greater fraction of the polymer at the nanocrystal interface, thereby minimizing the number of non-selective pathways for gas transport. Despite attempts to synthesize smaller Mg_2(dobdc) and Mn_2(dobdc) nanocrystals, these frameworks were always found to agglomerate during synthesis.

The differences between these two types of composite membrane are illustrated in Fig. 2b. From the cross-sectional view of the membrane, the Ni_2(dobdc) and Co_2(dobdc) nanocrystals are well dispersed. Conversely, Mg_2(dobdc) and Mn_2(dobdc) crystals do not interact as strongly with the polymer, resulting in interfacial gaps that contribute to non-selective gas transport. Scanning and transmission electron microscopy images (Fig. 3 and Supplementary Fig. 1) support these depictions, revealing agglomerations and interfacial gaps for the Mg_2(dobdc) and Mn_2(dobdc) membranes, whereas the film cross-sections are smooth and gaps are not apparent for the Co_2(dobdc) and Ni_2(dobdc) membranes. These results imply that the external surface functionality of the M_2(dobdc) nanocrystals plays a crucial role in their interactions with the polymer. Importantly, the nanocrystals necessarily have exposed surface metal sites capable of directly binding the polymer, and, in accord with the Irving–Williams stability order, the strength of those interactions can be expected to increase along the series Mg < Mn ≪ Co < Ni. The precise nature of these nanocrystal–polymer interactions was not readily apparent by infrared spectroscopy (Supplementary Fig. 4), although this is perhaps not surprising, because the overall percentage of coordinated polymer units is expected to be small.

Membrane dissolution studies using Soxhlet extraction were performed to probe directly the strength and abundance of these interfacial interactions (Fig. 4a). The 6FDA-DAM polymer is fully soluble in dichloromethane during membrane casting, and, as expected, the neat polymer membrane readily dissolved back into its casting solvent. Similarly, films loaded with Mg_2(dobdc)

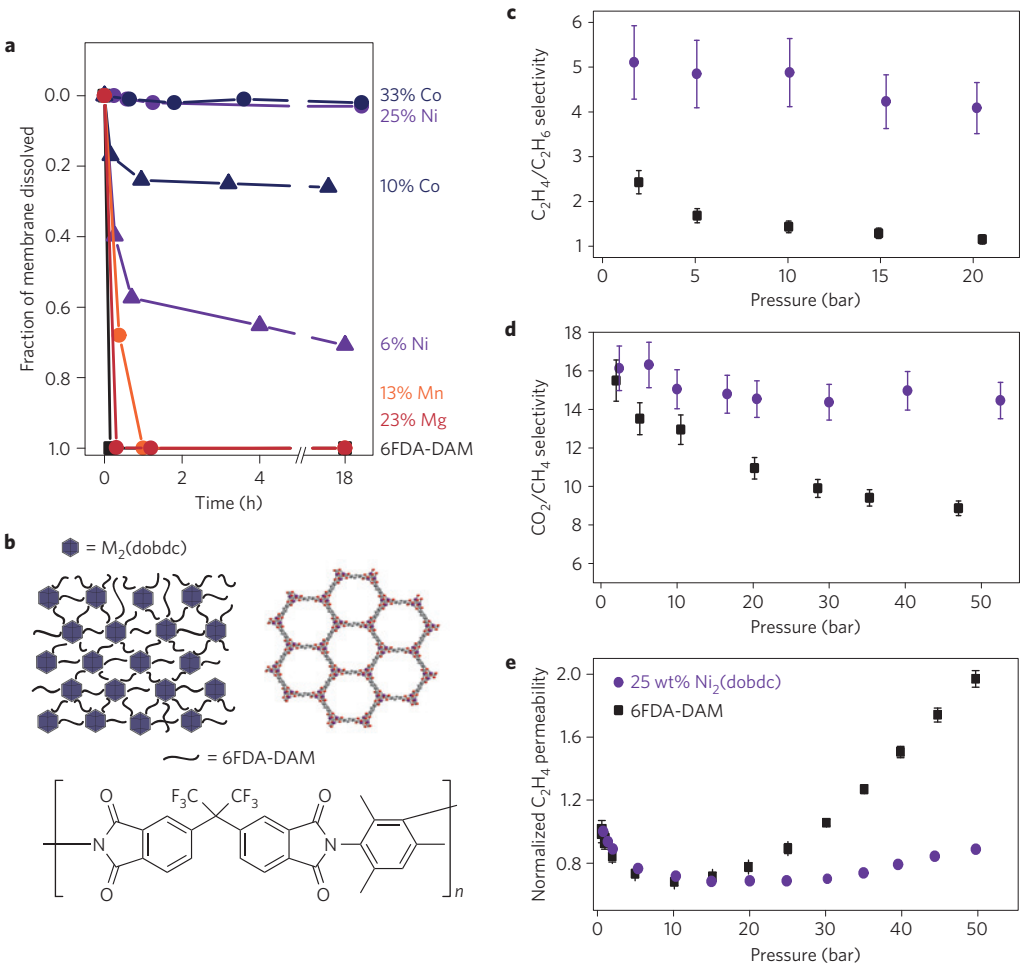

Figure 4 | Enhanced membrane stability, reduction in plasticization and high mixed-gas selectivities. a, Quantification of membrane stability by Soxhlet extraction in refluxing dichloromethane. The fraction of membrane dissolved corresponds to the mass of membrane remaining after a given period of time in the extractor relative to the initial mass. **b**, Illustration of the nanocrystal-induced polymer rigidification, along with the structures of M_2(dobdc) and 6FDA-DAM. **c**,**d**, Mixed-gas permeation data for a 50:50 C_2H_4/C_2H_6 (**c**) and a 50:50 CO_2/CH_4 mixture (**d**). Error bars correspond to propagation of uncertainty from the mass spectrometer calibration. **e**, Single-component C_2H_4 permeabilities, normalized to the permeability measured at 0.75 bar. Uncertainty in permeability corresponds to propagation of error from uncertainty in the film thickness, area and feed pressure. All permeabilities were collected at 35 °C, and steady-state permeation values were taken after six time lags. The composition was sampled from permeate that accumulated after steady-state permeation was reached. Permeability and selectivity data correspond to neat 6FDA-DAM (black squares) and 25% Ni_2(dobdc)/6FDA-DAM (purple circles). Raw permeability data are shown in Supplementary Fig. 9.

or Mn_2(dobdc) also rapidly dissolved. However, membranes incorporating Ni_2(dobdc) or Co_2(dobdc) nanocrystals were found to be partially or completely insoluble under the same conditions. At the highest loadings of 33 and 25 wt%, respectively, no membrane dissolution was observed after 18 h, which implies that framework–polymer interactions are so abundant for Co_2(dobdc) and Ni_2(dobdc) films that the stability of the membrane is enhanced. In further support of this conclusion, the polymer glass transition temperature was observed to increase from 393 to 397 °C on addition of Ni_2(dobdc) (Supplementary Table 2), indicating that the polymer is more rigid when in contact with the nanocrystals. Figure 4b shows an illustration of the two types of M_2(dobdc) nanocrystal–polymer interactions we have observed for our samples, one with strong interactions and a homogeneous nanocrystal distribution, and the other with weaker interactions and nanocrystal agglomerations.

When polymer chains are mobile, a membrane is highly susceptible to plasticization, because the interaction with a penetrating gas can have a solvating effect on the polymer, thereby disrupting interchain interactions. Modifying the interchain interactions to reduce chain mobility, as occurs on incorporating Co_2(dobdc) and Ni_2(dobdc) nanocrystals within 6FDA-DAM, should act to create plasticization resistance. To investigate this, we tracked the plasticization pressure response of these membranes for three strongly polarizable gases. In addition to ethylene and ethane, we chose to study CO_2 to compare with other studies on membrane plasticization[10]. Because permeability is normalized to the upstream pressure, the permeability of a non-plasticizing gas such as CH_4 or N_2 will decrease slightly (Supplementary Fig. 5) on increasing the pressure. If a plasticizing gas is tested in a permeation experiment, at a certain pressure, the permeability will begin to increase, and this pressure is known as the plasticization pressure. To a first approximation, a membrane with a higher plasticization pressure has a stronger resistance to plasticization than a membrane with a lower plasticization pressure[29]. For membranes containing Ni_2(dobdc) nanocrystals, we observed an enhanced resistance to plasticization (Fig. 4c–e and Supplementary Figs 5 and 9), as indicated by an increase in the plasticization pressure. For ethylene, ethane and CO_2, the plasticization pressure shifted from ~10 bar for the pure polymer to greater than 20 bar for the

nanocrystal-loaded films. Although an increase in the plasticization pressure is indicative of a reduction in membrane plasticization, the retention of high mixed-gas selectivities with increasing feed pressure is more conclusive. The permeation of equimolar mixtures of ethylene/ethane or CO_2/CH_4 was tested on 6FDA-DAM as well as 25 wt% Ni_2(dobdc). Owing to membrane plasticization, 6FDA-DAM becomes nearly non-selective for ethylene/ethane at 20 bar feed pressure, and the selectivity for CO_2/CH_4 drops from 15.5 (1.0) at 2 bar feed pressure to 8.9 (0.4) at 47 bar. On incorporation of Ni_2(dobdc), no reduction in selectivities were observed under high-pressure, mixed-gas conditions. For the nanocrystal composite, selectivities of 4.1 (0.6) at 20.5 bar of ethylene/ethane and 14.5 (0.9) at 52.5 bar of CO_2/CH_4 were observed. These values are similar to the pure-gas C_2H_4/C_2H_6 selectivities, and the CO_2/CH_4 selectivity has increased relative to the pure-gas values. The rare and beneficial effect of increasing permselectivity under mixed-gas conditions is potentially caused by strong competitive adsorption of CO_2 over CH_4 at the open metal site. To the best of our knowledge, this is the first demonstration of a composite material that suppresses plasticization without losses in permeability or selectivity. Even more importantly, industrial ethylene/ethane separations would ideally be conducted near saturation pressure. Whereas most neat polymer membranes are non-selective under these conditions, the composite materials presented here retain selectivity under a relevant feed environment.

Through a combination of increasing adsorptive selectivity, boosting permeability, and introducing strong framework–polymer interactions, our findings demonstrate that Co_2(dobdc) and Ni_2(dobdc) nanocrystals can greatly enhance the ethylene/ethane separation performance of a polymer membrane, placing these new composite materials well above the polymer upper bound. The presence of strong and abundant nanocrystal–polymer interactions not only benefits the intrinsic gas separation properties, but also suppresses plasticization by reducing polymer chain mobility. This strategy of enhancing membrane stability to highly polarizable gases through the incorporation of metal–organic framework nanocrystals with appropriate size and surface chemistry should be generally applicable to many other gas separations that involve plasticizing gases, potentially allowing membrane processes to be explored for key separations that were previously out of reach.

Methods

Methods and any associated references are available in the online version of the paper.

Received 2 September 2015; accepted 8 March 2016; published online 11 April 2016

References

1. *Materials for Separation Technology: Energy and Emission Reduction Opportunities* (US Department of Energy, 2005).
2. Eldridge, R. B. Olefin/paraffin separation technology: a review. *Ind. Eng. Chem. Res.* **32,** 2208–2212 (1993).
3. Rungta, M., Zheng, C. & Koros, W. J. Membrane-based ethylene/ethane separation: the upper bound and beyond. *AIChE J.* **59,** 3475–3489 (2013).
4. Baker, R. W. & Low, B. T. Gas separation membrane materials: a perspective. *Macromolecules* **47,** 6999–7013 (2014).
5. Peng, Y. *et al*. Metal–organic framework nanosheets as building blocks for molecular sieving membranes. *Science* **346,** 1356–1359 (2014).
6. Celebi, K. *et al*. Ultimate permeation across atomically thin porous graphene. *Science* **344,** 289–292 (2014).
7. Li, H. *et al*. Ultrathin, molecular-sieving graphene oxide membranes for selective hydrogen separation. *Science* **342,** 95–98 (2013).
8. Brown, A. J. *et al*. Interfacial processing of metal–organic framework hollow fiber membranes. *Science* **345,** 72–75 (2014).
9. Park, H. B. *et al*. Polymers with cavities tuned for fast selective transport of small molecules and ions. *Science* **318,** 254–258 (2007).
10. Wind, J. D., Staudt-Bickel, C., Paul, D. R. & Koros, W. J. The effects of crosslinking chemistry on CO_2 plasticization of polyimide gas sepation membranes. *Ind. Eng. Chem. Res.* **41,** 6139–6148 (2002).
11. Bloch, E. D. *et al*. Hydrocarbon separations in a metal–organic framework with open iron(II) coordination sites. *Science* **335,** 1606–1610 (2012).
12. Qiu, S., Xue, M. & Zhu, G. Metal–organic framework membranes: from synthesis to separation application. *Chem. Soc. Rev.* **43,** 6116–6140 (2014).
13. Zhang, C., Dai, Y., Johnson, J. R., Karvan, O. & Koros, W. J. High performance ZIF-8/6FDA-DAM mixed-matrix membranes for propylene/propane separations. *J. Membr. Sci.* **389,** 34–42 (2012).
14. Rodenas, T. *et al*. Metal–organic framework nanosheets in polymer composite materials for gas separation. *Nature Mater.* **14,** 48–55 (2015).
15. Bae, T.-H. & Long, J. R. CO_2/N_2 separations with mixed-matrix membranes containing Mg_2(dobdc) nanocrystals. *Energy Environ. Sci.* **6,** 3565–3569 (2013).
16. Liu, C., McCulloch, B., Wilson, S. T., Benin, A. I. & Schott, M. E. Metal organic framework-polymer mixed matrix membranes. US patent 7,637,983 B1 (2009).
17. Ranjan, R. & Tsapatsis, M. Microporous metal organic framework membrane on porous support using the seeded growth method. *Chem. Mater.* **21,** 4920–4924 (2009).
18. Seoane, B. *et al*. Metal–organic framework based mixed matrix membranes: a solution for highly efficient CO_2 capture? *Chem. Soc. Rev.* **44,** 2421–2454 (2015).
19. Venna, S. R. *et al*. Fabrication of MMMs with improved gas separation properties using externally-functionalized MOF particles. *J. Chem. Mater. A* **3,** 5014–5022 (2015).
20. Ploegmakers, J., Japip, S. & Nijmeijer, K. Mixed matrix membranes containing MOFs for ethylene/ethane separation Part A: Membrane preparation and characterization. *J. Membr. Sci.* **428,** 445–453 (2013).
21. Bux, H., Chmelik, C., Krishna, R. & Caro, J. Ethylene/ethane separation by the MOF membrane ZIF-8: molecular correlation of permeation, adsorption, diffusion. *J. Membr. Sci.* **369,** 284–289 (2011).
22. Herm, Z. R., Bloch, E. D. & Long, J. R. Hydrocarbon separations in metal–organic frameworks. *Chem. Mater.* **26,** 323–338 (2014).
23. Bae, Y.-S. *et al*. High propene/propane selectivity in isostructural metal–organic frameworks with high densities of open metal sites. *Angew. Chem. Int. Ed.* **51,** 1857–1860 (2012).
24. Bloch, E. D. *et al*. Selective binding of O_2 over N_2 in a redox-active metal-organic framework with open iron(II) coordination sites. *J. Am. Chem. Soc.* **133,** 14814–14822 (2011).
25. Rosi, N. L. Rod packings and metal–organic frameworks constructed from rod-shaped secondary building units. *J. Am. Chem. Soc.* **127,** 1504–1518 (2005).
26. Geier, S. J. *et al*. Selective adsorption of ethylene over ethane and propylene over propane in the metal-organic frameworks M_2(dobdc) (M = Mg, Mn, Fe, Co, Ni, Zn). *Chem. Sci.* **4,** 2054–2061 (2013).
27. Caskey, S. R., Wong-Foy, A. G. & Matzger, A. J. Dramatic tunic of carbon dioxide uptake via metal substitution in a coordination polymer with cylindrical pores. *J. Am. Chem. Soc.* **130,** 10870–10871 (2008).
28. Tanaka, K., Taguchi, A., Hao, J., Kita, H. & Okamoto, K. Permeation and separation properties of polyimide membranes to olefins and paraffins. *J. Membr. Sci.* **121,** 187–207 (1996).
29. Bos, A., Punt, I. G. M., Wessling, M. & Strathmann, H. CO_2-induced plasticization in glassy polymers. *J. Membr. Sci.* **31,** 67–78 (1999).

Acknowledgements

This research was supported through the Center for Gas Separations Relevant to Clean Energy Technologies, an Energy Frontier Research Center funded by the US Department of Energy, Office of Science, Office of Basic Energy Sciences under Award DE-SC0001015. We thank J. Mason for helpful discussions. We also thank the NSF for providing graduate fellowship support for J.E.B.

Author contributions

J.E.B. and J.R.L. formulated the project. J.E.B. synthesized nanocrystals and fabricated membranes. Z.P.S. contributed valuable theoretical insights, synthesized 6FDA-DAM, and assisted in construction of permeation equipment. J.E.B. collected all powder diffraction, dynamic light scattering, scanning electron microscopy, Soxhlet extractions, gas adsorption, and gas permeation data. T.L. performed transmission electron microscopy imaging. J.E.B. and J.R.L. wrote the paper, and all authors contributed to revising the paper.

Additional information

Supplementary information is available in the online version of the paper. Reprints and permissions information is available online at www.nature.com/reprints. Correspondence and requests for materials should be addressed to J.R.L.

Competing financial interests

The authors declare no competing financial interests.

Methods

Synthesis of M_2(dobdc) nanocrystals. All nanocrystal syntheses were conducted at room temperature. Solid 2,5-dihydroxyterephthalic acid (1.0 g, 5.0 mmol; H_4(dobdc)) and 16 mmol of $M(NO_3)_2 \cdot 6H_2O$ (M = Mg, Co, Ni) or $MnCl_2 \cdot 4H_2O$ were added to a mixture of 400 ml of dimethylformamide (DMF), 27 ml of ethanol, and 27 ml of water in a 500-ml round bottom flask. After sparging the mixture with N_2, 5 ml of triethylamine was added rapidly while stirring under an N_2 atmosphere. The M_2(dobdc) nanocrystals precipitated within minutes, but all reaction mixtures were stirred for 2 h. The suspended M_2(dobdc) nanoparticles were immediately collected by centrifugation, the solid was redispersed in 250 ml of DMF, and the suspension was heated at 120 °C for 6 h. The centrifugation and DMF washing steps were repeated five times to remove unreacted ligand. The nanocrystals were then collected by centrifugation, redispersed in 250 ml of methanol, and the suspension was heated at 60 °C for 2 h. The centrifugation and methanol washing steps were repeated five times to exchange all of the DMF for methanol, including those molecules coordinated to the metal sites. Full removal of DMF was confirmed by infrared spectroscopy. Nanocrystals were then stored in methanol until membrane casting, or dried under reduced pressure at 180 °C for 24 h before gas adsorption measurements.

Membrane casting and activation. To prevent agglomeration, nanocrystals were not dried before film casting and formation. Concentrations of M_2(dobdc) in methanol were determined by sonicating a stock solution and reducing a 1-ml aliquot to dryness to find the mass of activated nanocrystals, and resulting stock solutions were found to be ~50 mg ml^{-1}. For M_2(dobdc)/6FDA-DAM mixed-matrix membranes, an aliquot from the M_2(dobdc) stock solution in methanol was taken and redispersed in 10 ml of dichloromethane. The nanocrystal suspension was then sonicated using a horn sonicator for 1 min, adding additional dichloromethane to maintain a total volume of 10 ml. 6FDA-DAM was then dissolved into the M_2(dobdc) suspension and the mixture was sonicated for another 1 min. The mixture was cast onto a glass plate and the dichloromethane was allowed to evaporate over the course of ~24 h—the resulting films were found to be 40–70 μm thick. The freestanding film was then dried in a vacuum oven at 120 °C for 24 h to remove residual dichloromethane.

The loading of M_2(dobdc) nanocrystals in 6FDA-DAM was determined by a thermogravimetric analysis method. For reference, the M_2(dobdc) powder was first activated under flowing N_2 at 180 °C for 1.5 h to ensure activation, and then the samples were heated to 600 °C under flowing O_2. The remaining oxide mass was compared to the initial activated mass of the metal–organic framework. Results are presented in Supplementary Fig. 6. The same procedure was conducted for the M_2(dobdc)/6FDA-DAM films. The percentage of mass remaining after the ramp to 600 °C under O_2 is attributable to metal oxide, and from this the amount of activated M_2(dobdc) present in the film was obtained.

Gas permeability measurements. Gas permeation was determined using permeation systems that were constructed in-house. To prepare samples, films were supported on brass shim stock disks. These disks were machined to fit tightly into our permeation cells, and they contained a hole bored directly through their centre. Films were placed over the hole, and a seal was formed between the brass disk and film by affixing samples to the disk with an impermeable polydimethylsiloxane (PDMS) glue. On curing, a small area of film remained exposed, and the area of film accessible to gas transport was determined using a scanner. Membrane thicknesses were measured with a depth gauge. The membrane support was loaded into a stainless steel filter holder (Millipore XX4502500 for single low-pressure measurements, Millipore XX4504700 for multiple high-pressure single-component measurements, and Millipore XX4404700 for high-pressure mixed-gas measurements). To activate the M_2(dobdc) nanocrystals contained within the polymer membrane, the film was heated at 180 °C *in situ* under dynamic vacuum for ~12 h using a custom-built heating mantle. Before gas permeation tests, the system was held under static vacuum and the leak rate into the downstream volume was determined. This leak rate was then subtracted from subsequent permeation rates; however, we note that the leak rate was <1% of the permeation rate for each of the gases tested. For single-point, low-pressure measurements, ethane permeation tests were run before ethylene, and samples were reactivated at 180 °C for 30 min in between measurements. The same film was used for each gas to prevent uncertainty in membrane thickness or exposed area from translating into uncertainty in selectivity. To ensure that our results were independent of thermal annealing history, as well as plasticization and conditioning effects, permeation experiments were repeated on films that were previously exposed to ethane and ethylene, and, within the uncertainty of the measurements, no changes were observed in permeation for the second set of experiments. In the case of high-pressure measurements, where membranes are susceptible to plasticization, a new membrane was loaded, so that plasticization of the film by the previous gas did not affect the permeability measurements after each plasticizing gas—that is, CO_2, C_2H_4 and C_2H_6. Permeation tests were run for at least six times the time lag at each pressure point (the time lag is defined in the Supplementary Information). For permeation tests where a time lag was not detectable, permeation was measured for 3 min at each pressure point. In measuring mixed-gas permeation, a similar procedure to high-pressure single-component measurements was followed. To prevent concentration polarization on the feed side of the membrane, the gas mixture (either 50:50 C_2H_4 in C_2H_6 or 50:50 CO_2 in CH_4) was flowed across the feed side of the film, through a needle valve and a bubbler. The ratio of the permeation rate to the feed sweep rate, or stage cut, was kept at <1%. The gas mixture was allowed to permeate the membrane until a steady-state permeation rate was reached (>6 time lags). The permeate volume was then evacuated and allowed to accumulate under steady-state conditions. The permeate gas was then expanded into an evacuated volume and analysed with a mass spectrometer (MKS Microvision 2). To determine the fraction $p_{C_2H_4}/(p_{C_2H_4}+p_{C_2H_6})$, the mass fraction of (mass 27)/[(mass 27) + (mass 30)] was calibrated to cylinder mixtures of known composition. Similarly, to determine $p_{CO_2}/(p_{CO_2}+p_{CH_4})$, the mass fraction of (mass 44)/[(mass 44) + (mass 15)] was used. Calibration curves for these mixtures are given in Supplementary Figs 12 and 13. The uncertainty in the downstream mole ratio is a propagation of uncertainty from the standard error in the mole ratio calibration.

Gas adsorption measurements. Low-pressure gas adsorption data between 0 and 1.1 bar were measured using a Micromeritics ASAP 2020 instrument. Samples consisting of 50-100 mg of M_2(dobdc) powder, polymer film, or mixed-matrix film were loaded into a preweighed tube, and heated at 180 °C for 24 h. The mass of the activated sample was then used as the basis for the adsorption measurements. After an adsorption isotherm was measured, the sample was reactivated at 180 °C for 3 h before measuring a subsequent adsorption isotherm.

Imaging of mixed-matrix membranes and M_2(dobdc) nanocrystals. For cross-sectional transmission electron microscopy (TEM) samples, the mixed-matrix membranes were imbedded in epoxy resin (Araldite 502, Electron Microscopy Sciences) and cured at 60 °C for 12 h. The sample was then cut into ~100-nm-thick sections using an RMC MT-X Ultramicrotome (Boeckeler Instruments) and collected on copper TEM grids. TEM images were obtained on a JEOL 1200 EX TEM instrument operating at an accelerating voltage of 120 kV. Scanning electron microscopy (SEM) images were collected at 5 keV/12 μA using a field emission SEM instrument (JEOL FSM6430). Membrane cross-sections were exposed by fracturing in liquid nitrogen. For imaging M_2(dobdc) powders, SEM samples were prepared by dispersing the nanocrystals in dichloromethane and drop casting onto a silicon chip. To dissipate charge, the samples were sputter coated with ~3 nm of Au (Denton Vacuum, LLC). TEM samples of M_2(dobdc) powders were prepared by dispersing nanocrystals into methanol and drop casting onto copper TEM grids.

Determination of glass transition temperatures. The glass transition temperature (T_g) for 6FDA-DAM, 6 wt% Ni_2(dobdc) and 25 wt% Ni_2(dobdc) were determined by differential scanning calorimetry using a TA Q200 instrument. Temperature scans were conducted at 10 °C min^{-1} between 40 and 410 °C, and the exotherm on the second temperature scan was taken for the T_g.

Dynamic light scattering measurements. Number-averaged particle size distributions were collected by dynamic light scattering. After synthesis, including washing in methanol, a 1-mg sample of the M_2(dobdc) nanocrystals was suspended in 20 ml of methanol and sonicated using a horn sonicator for 2 min. Measurements were performed at 35 °C on a Brookhaven BI-200sm instrument, using samples suspended in methanol and assuming a refractive index of 1.7 for the M_2(dobdc) nanocrystals.

Calculating permeability. To ensure steady-state permeation rates are attained, permeability measurements were run for at least six times the time lag, where the time lag is defined as the intercept on the time-axis on the pressure versus time plot where a line is drawn fitting the linear region[30]. $t = 0$ corresponds to when the downstream volume is closed to vacuum and the gas is allowed to begin accumulating. At the end of six times the time lag, the slope of the line fitting the last 20% of the data was used to determine the steady-state permeation rate. In the case that the time lag was not detectable, that is, for CO_2 permeation, the permeation at each pressure point was allowed to proceed for 3 min.

The pressure-based permeability is calculated using equation (1), where P is the permeability, l is the thickness of the film, V_{cell} is the volume downstream of the membrane where gas is allowed to accumulate during a permeation test, A is the area of the membrane exposed to permeation, P_f is the upstream pressure, R is the gas constant, T is the temperature in kelvin, $(dp/dt)_{ss}$ is the steady-state permeation rate, and $(dp/dt)_{leak}$ is the leak rate. We report permeabilities in the unit of Barrer (1 Barrer = 10^{-10} (cm^3(STP) cm)/(cm^2 s cmHg)).

$$P = \frac{lV_{cell}}{Ap_fRT}[(dp/dt)_{ss} - (dp/dt)_{leak}] \quad (1)$$

Uncertainty in the permeability was propagated from uncertainty in the film thickness, film area, upstream pressure transducer, temperature and downstream volume.

Calculation of permeability based on upstream fugacity. The true driving force for the permeation of gas is the gradient in the chemical potential across the membrane. Normally, pressure is used as a proxy for the chemical potential and is valid in the limit of $P \rightarrow 0$. At higher pressures, however, the pressure no longer remains an adequate proxy for the driving force because non-ideal gas behaviour becomes significant. Instead, the gas fugacity is a more accurate measure of the imposed driving force for permeation.

The fugacity-based permeability can be calculated by

$$P = \frac{lV_{cell}}{Af_f RT}[(dp/dt)_{SS} - (dp/dt)_{leak}] \quad (2)$$

where f_f is the fugacity of the feed.

This treatment is especially relevant for polarizable gases, for example, CO_2, C_2H_4 and C_2H_6, where the fugacity deviates strongly from the pressure at the conditions tested here. Fugacities were estimated from the virial equation using both second and third virial coefficients. Second virial coefficients were taken from the polynomial expressions recommended by Dymond *et al.*, and third virial coefficients were estimated from data tables compiled by Dymond *et al.* by plotting multiple data points around 35 °C (ref. 31). The plots were fitted to polynomial expressions, and the best fit value was taken at 35 °C. Gas density data was taken from REFPROP, which is a database maintained by NIST[32].

Because pressure overestimates the driving force for permeation, the fugacity-based permeability isotherm tends to turn upwards at higher fugacities as compared to the pressure-based permeability isotherm. This trend results in a lower experimental plasticization point compared to the pressure-based permeability data. It is important to note, however, that reduction in the plasticization is still clearly observed for each case (Supplementary Figs 10 and 11), regardless of the basis for permeability calculations.

Calculation of permeability parameters. To further elucidate the mechanism of increased selectivity and permeability, it was useful to determine the relevant parameters contributing to the permeability. Assuming that permeation follows the solution-diffusion model in these films,

$$P = DS \quad (3)$$

where D is the diffusivity in $cm^2\ s^{-1}$ and S is the solubility in $(cm^3(STP)/(cm^3\ mbar))$. The solubility is also related to the equilibrium adsorption isotherm,

$$S = \frac{\rho n_o}{p_o} \quad (4)$$

where ρ is the density of the membrane in $g\ cm^{-3}$, n_o is the amount adsorbed in equilibrium with the feed pressure in $cm^3(STP)\ g^{-1}$, and measured from the adsorption isotherm, and p_o is the feed pressure in mbar. The density of the membrane was calculated using the crystallographic density of the framework[33], the density of the polymer, and the mass loading of M_2(dobdc) in the polymer as measured by TGA. The diffusivity can then by calculated using $D = P/S$.

Alternatively, the diffusivity can be calculated using the time-lag method,

$$D = \frac{l^2}{6\theta} \quad (5)$$

where θ is the time lag[30]. These diffusivities are presented in Supplementary Table 3. Interestingly, the diffusivities as calculated from the time-lag method are lower than for the static, solution-diffusion calculation. This result can be explained by the much higher adsorption enthalpy on the open metal sites of the framework causing partial immobilization of the penetrant during non-steady-state permeation[34].

Polymer synthesis. Polyimides were formed from 2,2′-bis-(3,4-dicarboxyphenyl) hexafluoropropane dianhydride (6FDA) and diaminomesitylene (DAM) using standard chemical imidization techniques[35,36]. The dianhydride, 6FDA (P/N H0771, CAS # 1107-00-2), and diamine, DAM (P/N T1275, CAS # 3102-70-3), were purchased from TCI. Before use, 6FDA was purified once by vacuum sublimation and DAM was purified three times by vacuum sublimation. N-methyl-2-pyrrolidone (NMP) was purchased from Spectrum Chemicals (P/N M1557) and vacuum distilled immediately before use. Triethylamine (P/N TX1200-5) and acetic anhydride (P/N 320102) were purchased from EMD and Sigma-Aldrich, respectively, and were used as received. A dry atmosphere was maintained within the reaction glassware by flowing house nitrogen through a Drierite column (W.A. Hammond Drierite) upstream of the reaction vessel. All glassware was attached to flowing, dry nitrogen before being flame dried.

To a three-neck flask equipped with overhead mechanical stirrer, 2.152 g (14.33 mmol) of DAM was added and dissolved in 15 ml of NMP. Following dissolution of the diamine, the three-neck flask was cooled to 0 °C using an ice bath before slowly adding 6.364 g (14.33 mmol) of 6FDA and an additional 15 ml of NMP. The sample was stirred for approximately 24 h to form a viscous poly(amic acid). Next, approximately 2 ml of triethylamine and 5.4 ml of acetic anhydride were added as the activating and dehydrating agents, respectively, for chemical imidization. The solution was diluted with an additional 6 ml of NMP and allowed to stir for a further 20 h to form the polyimide.

Following imidization, the viscous polymer solution was precipitated by pouring the reaction solution slowly into approximately 1 l of methanol (MeOH), which was stirring at intermediate speeds on a stir plate. The polymer fibres were rinsed thoroughly with MeOH, placed in a fresh batch of MeOH, and stirred to extract residual reaction solvent for approximately 18 h. Next, the fibres were again thoroughly rinsed in fresh MeOH before stirring the sample in fresh MeOH for a further 18 h. After a final filtration and drying step, the polymer fibres were heated at 225 °C for approximately 24 h under vacuum. Following these rinsing and drying steps, no solvent was observed in the polymer film as determined from thermogravimetric analysis.

NMR. ^{1}H NMR was run on a 400 MHz instrument using $CDCl_3$ as the solvent. Supplementary Fig. 7 presents the spectra, and the peak assignments closely match those reported in the literature[37]. In addition to the peak for $CDCl_3$ (7.30 ppm), a peak for water appears at 2.14 ppm. No peaks were observed between 10 and 12 ppm, which indicates that the poly(amic acid) was fully imidized[38].

GPC. Molecular weight was estimated using a Viscotek TDA 302 size exclusion chromatography (SEC) system calibrated relative to polystyrene and using tetrahydrofuran (THF) as the solvent. Supplementary Table 4 presents the weight-averaged molecular weight, number-averaged molecular weight, and polydispersity index for the sample considered in this study.

References

30. Frisch, H. L. The time lag in diffusion. *J. Phys. Chem.* **61,** 93–95 (1957).
31. Dymond, J. H., Marsh, K. N., Wilhoit, R. C. & Wong, K. C. (eds) *The Virial Coefficients of Pure Gases and Mixtures* Vol. IV (Oxford Univ. Press, 2001).
32. Lemmon, E. W., Huber, M. L. & McLinden, M. O. *NIST Standard Reference Database 23: NIST Reference Fluid Thermodynamic and Transport Properties (REFPROP)* Version 8.0 (NIST, 2007).
33. Queen, W. L. *et al*. Comprehensive study of carbon dioxide adsorption in metal-organic frameworks M_2(dobdc) (M = Mg, Mn, Fe, Co, Ni, Cu, Zn). *Chem. Sci.* **5,** 4569–4581 (2015).
34. Paul, D. R. & Koros, W. J. Effect of partially immobilizing sorption on permeability and the diffusion time lag. *J. Polym. Sci.* **14,** 675–685 (1976).
35. Ohya, H., Kudryavtsev, V. V. & Semenova, S. I. *Polyimide Membranes: Applications, Fabrications, and Properties* (Gordon and Breach, 1996).
36. Ghosh, M. K. & Mital, K. L. *Polyimides: Fundamentals and Applications* (Marcel, 1996).
37. Grubb, T. L. *et al*. Highly soluble polyimides from sterically hindered diamines. *Polymer* **40,** 4279–4288 (1999).
38. Matsuura, T., Hasuda, Y., Nishi, S. & Yamada, N. Polyimide derived from 2,2′-bis (triflouromethyl)-4,4′-diaminobiphenyl. S. synthesis and characterization of polyimides prepared with 2,2′-bis (3,4-dicarboxyphenyl)hexafluoropropane dianhydride or pyromellitic dianhydride. *Macromolecules* **24,** 5001–5005 (1991).